Environmental Science & Technology

pubs.acs.org/est

Article

Mapping Yearly Fine Resolution Global Surface Ozone through the Bayesian Maximum Entropy Data Fusion of Observations and Model Output for 1990–2017

Marissa N. DeLang, Jacob S. Becker, Kai-Lan Chang, Marc L. Serre, Owen R. Cooper, Martin G. Schultz, Sabine Schröder, Xiao Lu, Lin Zhang, Makoto Deushi, Beatrice Josse, Christoph A. Keller, Jean-François Lamarque, Meiyun Lin, Junhua Liu, Virginie Marécal, Sarah A. Strode, Kengo Sudo, Simone Tilmes, Li Zhang, Stephanie E. Cleland, Elyssa L. Collins, Michael Brauer, and J. Jason West*

Cite This: *Environ. Sci. Technol.* 2021, 55, 4389–4398

Read Online

ACCESS | Metrics & More | Article Recommendations | Supporting Information

ABSTRACT: Estimates of ground-level ozone concentrations are necessary to determine the human health burden of ozone. To support the Global Burden of Disease Study, we produce yearly fine resolution global surface ozone estimates from 1990 to 2017 through a data fusion of observations and models. As ozone observations are sparse in many populated regions, we use a novel combination of the M^{3}Fusion and Bayesian Maximum Entropy (BME) methods. With M^{3}Fusion, we create a multimodel composite by bias-correcting and weighting nine global atmospheric chemistry models based on their ability to predict observations (8834 sites globally) in each region and year. BME is then used to integrate observations, such that estimates match observations at each monitoring site with the observational influence decreasing smoothly across space and time until the output matches the multimodel composite. After estimating at 0.5° resolution using BME, we add fine spatial detail from an additional model, yielding estimates at 0.1° resolution. Observed ozone is predicted more accurately (R^2 = 0.81 at the test point, 0.63 at 0.1°, and 0.62 at 0.5°) than the multimodel mean (R^2 = 0.28 at 0.5°). Global ozone exposure is estimated to be increasing, driven by highly populated regions of Asia and Africa, despite decreases in the United States and Russia.

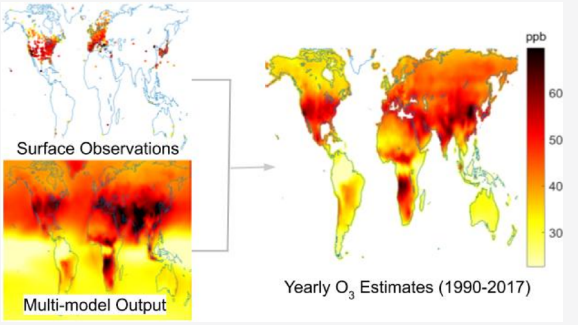

INTRODUCTION

Tropospheric ozone is harmful to human health through respiratory and cardiovascular health effects associated with short- and long-term exposure.[1−3] Additionally, tropospheric ozone influences climate[4] and damages plant growth.[5,6] Surface ozone estimates at fine spatial resolution, which are required to determine the human health burden of ozone exposure, are typically based on two sources: monitoring networks and atmospheric chemistry models. Monitoring networks provide high spatial coverage of surface ozone observations in North America, Europe, Japan, South Korea, and recently China; however, stations are scarce elsewhere.[7] Global atmospheric models estimate concentrations across many years over all world regions; however, models have biases.[8]

The Global Burden of Disease (GBD) Study conducts a comparative risk assessment that estimates the health burden caused by specific risk factors from 1990 to the present day, updated regularly. Two ambient air pollution risk factors are analyzed: fine particulate matter ($PM_{2.5}$) and ozone.[9,10] GBD $PM_{2.5}$ estimates are generated through a combination of satellite retrievals and land use information with a single atmospheric model calibrated to surface observations with a Bayesian hierarchical model.[11,12] In contrast, global ozone estimates prior to GBD 2017[13] were provided by a single model with no bias correction to observations.[14] Satellite measurements provide $PM_{2.5}$ estimates at fine resolution but do not accurately detect surface ozone.[14,15]

The recent Tropospheric Ozone Assessment Report (TOAR) collected ozone observations from thousands of sites around the world, which made it possible to incorporate surface observations into GBD estimates.[7,16] For GBD 2017, TOAR observations were combined with six atmospheric models from phase one of the Chemistry-Climate Model Initiative (CCMI)[17] using the M^{3}Fusion method for the average of 2008 to 2014.[18] In M^{3}Fusion, models were bias-corrected and combined by finding the optimal linear combination of models in each world region, weighted based

Received: November 16, 2020
Revised: February 12, 2021
Accepted: February 16, 2021
Published: March 8, 2021

on their performance with respect to observations. Within two degrees of a monitoring station, the multimodel composite was then replaced with a spatial interpolation of observations. The 2008−2014 ozone distribution was extended backward (1990−2008) by scaling with cubic splines relative to prior GBD ozone estimates and forward (2014−2017) by extending the annual rate of change from 2012, for use in GBD 2017.[13]

While the M^{3}Fusion method significantly improved upon previous GBD ozone estimates, we identify a potential for further improvements. In particular, the correction within two degrees of an observation can create discontinuities, which could be improved by using advanced geostatistical techniques that combine model output with observations using smooth weighting across space. Here, we use a novel combination of the M^{3}Fusion and Bayesian Maximum Entropy (BME) methods,[19−22] which is uniquely suited to the challenges of mapping global ozone concentrations, as only observations and models provide useful information and observations are sparse in some world regions. The regional "large-scale" bias correction and weighting of models in the M^{3}Fusion multimodel composite provide the best estimate of ozone far from observations. Then, BME provides a local "small-scale" correction, by smoothly integrating observations in both space and time such that estimates match observations at the measurement site, and the influence of those observations decreases with distance according to the spatiotemporal covariance. Since ozone monitoring is inconsistent, allowing observations to affect predictions across time could provide more accurate estimates. Near observation locations, therefore, ozone estimates are strongly influenced by observations. BME was previously used to fuse ozone observations with models on state and national scales,[23−25] but it was not used previously globally. Apart from Chang et al.,[18] we are not aware of any global data fusion of ozone observations and models.

We aim to estimate global fine resolution (0.1°) surface ozone for each year from 1990 to 2017 to support the GBD 2019 Study by combining surface observations with multiple global atmospheric models by first using M^{3}Fusion to create multimodel composites and then applying BME to smoothly fuse multimodel composites with observations in space and time. We improve upon the single 7-year mean ozone fields produced for GBD 2017[18] by producing yearly output for 1990−2017, including additional observations and model output, smoothly weighting observations across space and time, and applying fine spatial structure based on fine resolution model output. To add fine spatial resolution for GBD, we apply the fine-scale spatial patterns from a global fine resolution model simulation.[26] Our annual global ozone maps were used by GBD 2019, which were extrapolated to 2019 using log-linear trends based on our 2008−2017 estimates, and estimated 365,000 (95% CI, 175,000−564,000) premature chronic obstructive pulmonary disease deaths globally or 6.21 (2.99−9.63) million disability-adjusted life years, from ambient ozone exposure in 2019.[27]

MATERIALS AND METHODS

M^{3}Fusion and BME are used in sequence to estimate global surface ozone concentrations. Other methods have been applied on smaller scales, such as neural networks using meteorological and emission variables to predict ozone,[28,29] but those relationships may not apply elsewhere.

GBD's ozone metric for quantifying health outcomes from long-term ozone exposure is the ozone season daily maximum 8 h mixing ratio (OSDMA8).[2] OSDMA8 is calculated as the annual maximum of the six-month running mean of the monthly average daily maximum 8 h mixing ratio, including through March of the following year to contain the Southern Hemisphere summer. All observations and model output are converted to OSDMA8 using the same algorithm, and estimates are reported here as OSDMA8.

Surface Ozone Observations. We include surface ozone observations from the TOAR and the Chinese National Environmental Monitoring Center (CNEMC) Network (Figure 1). The TOAR is the world's largest collection of in situ hourly surface ozone observations covering 1970−2015.[16,30] The database contains dense observations in North America, Europe, Japan, and South Korea and sparse observations elsewhere.[7] The database was updated for this project to include readily available datasets for the years 2015−2017, but measurements were not updated for all nations previously included. The CNEMC includes surface ozone observations for 2013−2017 in China,[31] which were quality-controlled using the algorithm that the TOAR applies elsewhere. The total observations ranged from a minimum of 1199 in 1990 to a maximum of 4999 in 2015. The incomplete TOAR update in 2016 and 2017 yielded fewer observation sites than 2015.

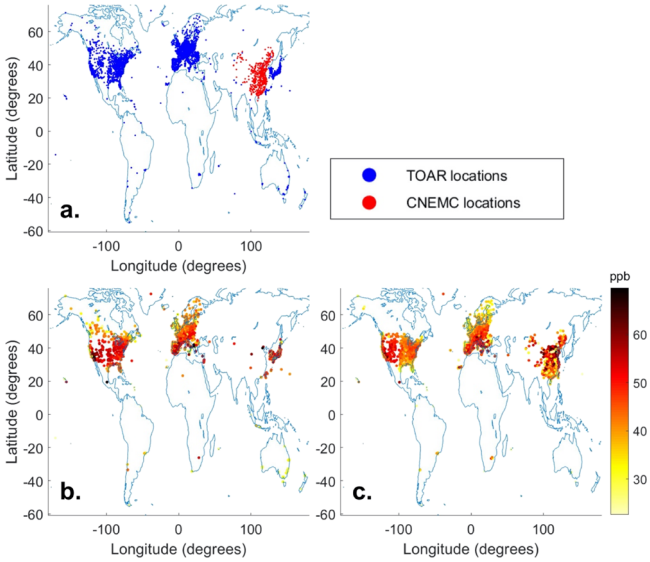

Figure 1. (a) TOAR and CNEMC monitoring locations with at least one valid yearly OSDMA8 observation over 1990−2017. In total, there are 8834 monitoring stations, 7269 from the TOAR and 1565 from the CNEMC. (b) Surface observations as OSDMA8 in 2005, with an average of 45.5 ppb and a maximum of 82.2 ppb in Mexico City, Mexico. (c) Surface observations as OSDMA8 in 2015, with an average of 46.2 ppb and a maximum of 80.9 ppb in Zibo, China.

Atmospheric Chemistry Model Simulations. We incorporate modeled ozone from nine atmospheric chemistry model simulations (Table 1). The models, mostly from CCMI,[17] report output for 1990−2010 from the specified dynamics REF-C1SD experiment,[17,32] which uses annual MACCity emissions.[33,34] Three models, MOCAGE, MERRA2-GMI, and GFDL-AM3, were extended past 2010. To increase models after 2010, we include output from the specified dynamics experiments of MRI-ESM2.0 and GFDL-AM4, for modified Coupled Model Intercomparison Project Phase 6 (CMIP6)[35] experiments.

https://dx.doi.org/10.1021/acs.est.0c07742
Environ. Sci. Technol. 2021, 55, 4389−4398

Table 1. Nine Atmospheric Chemistry Models Used in This Study

model	years	resolution	experiment	reference
CESM1 CAM4-Chem	1990−2010	1.9° × 2.5°	CCMI REF-C1SD	36
CESM1 WACCM	1990−2010	1.9° × 2.5°	CCMI REF-C1SD	37 and 38
CHASER	1990−2010	2.8° × 2.8°	CCMI REF-C1SD	39−41
GFDL AM3	1990−2014	2° × 2.5°	CCMI REF-C1SD	42−44
GFDL AM4	2010−2016	1° × 1.25°	CMIP6 nudged to NCEP winds[a]	45 and 46
MERRA2-GMI	1990−2017	0.5° × 0.625°	MACCity and GFED-4s emissions[b]	47 and 48
MOCAGE	1990−2016	2° × 2°	CCMI REF-C1SD	49 and 50
MRI-ESM1r1	1990−2010	2.8° × 2.8°	CCMI REF-C1SD	51
MRI-ESM2.0	2011−2017	2.8° × 2.8°	CMIP6 historical and ssp370[c]	52

[a]Nudged to observed meteorology similar to GFDL-AM3 and uses anthropogenic emissions modified from CMIP6 to reflect recent NO_x trends in China and the United States.[45] [b]MACCity anthropogenic emissions with biomass burning emissions from Global Fire Emissions Dataset version 4s.[47,48] [c]Emissions from the CMIP6 historical (2011−2014) and ssp370 (2015−2017) experiments.[52]

Multimodel Composite. We use M^{3}Fusion to create multimodel composites of the models available in each year from 1990 to 2017.[18] This method corrects for model bias and finds the linear combination of models in each region and year that minimizes the mean square error as compared to observations. Since model resolution varies, we use bilinear interpolation to smooth yearly OSDMA8 to a 0.5° × 0.5° grid. We interpolate yearly observations from irregular monitoring station locations to the 0.5° grid using the stochastic partial differential equation approach.[53] In each of the eight geographical regions (Figure S1) and each year, we weight each model to minimize the difference between the multimodel average and spatially interpolated observations based on a constrained least-squares approach

$$\begin{aligned}&\text{minimize}\\ &\{\alpha_r\beta_{rk};\ k = 1, \ldots, n\}\\ &\sum_{s_g \in \text{Region } r} \left(\hat{y}(s_g) - \alpha_r - \sum_{k=1}^{n} \beta_{rk}\eta_k(s_g)\right)^2, \text{ subject to}\\ &\sum_{k=1}^{n} \beta_{rk} = 1 \text{ and } \beta_{rk}\\ &\geq 0\end{aligned} \tag{1}$$

where s_g is the grid cell at 0.5° resolution, $\hat{y}(s_g)$ is the spatially interpolated observations, $\{\eta_k(s_g);\ k = 1,...,n\}$ is the model output on the same grid from the n models available, α_r is a constant that corrects overall bias in each region, and β_{rk} is an optimal weight for the kth model in region r. All model weights are constrained to be positive and sum to 1. The constant offset α_r guarantees that the residuals have a zero mean, through which the mean model bias is corrected in each region.[18]

Since M^{3}Fusion relies on spatially interpolated observations to determine model weights, we modify the method for data sparse regions and years. In North America and Europe, we use weights based on each individual year's models and observation values. For all other regions, we calculate individual year weights for 2000−2010 and apply weights from the aggregated 2000−2010 period to 1990−1999. For 2011−2017, East Asia uses individual year weights, while South America, Africa, South-Central Asia, Russia, and Oceania use weights from the aggregated 2011−2014 period, for which the TOAR dataset was complete.

Bayesian Maximum Entropy Methodology. BME is a geostatistical method that incorporates multiple forms of knowledge to predict an estimate of a homogeneous, stationary, space−time random field.[19−22] Using BME, we combine surface observations and annual multimodel composites to calculate an ozone estimate that matches observations at each monitoring station, and the observational influence gradually diminishes across space and time until it matches the multimodel composite. BME was described previously, including in the fusion of ozone observations with model output at state and national scales.[20−24,54] We model the offset-removed, homogeneous space−time random field (S/TRF) $X(\boldsymbol{p})$ at the space−time coordinate $\boldsymbol{p} = (s,t)$.[24] In BME, there are two forms of knowledge: site-specific and general. Site-specific knowledge can consist of hard data, with no assumed uncertainty, and soft, probabilistic data. Here, we only have hard data, which is the linear limiting case of the BME data integration framework.[24] We remove the offset, the multimodel composite at monitoring stations ($o_z(\boldsymbol{p}_0)$), from OSDMA8 observations ($\boldsymbol{z}_0$) at monitoring station locations $\boldsymbol{p}_0$ to obtain hard data $\boldsymbol{x}_0$

$$\boldsymbol{x}_0 = \boldsymbol{z}_0 - o_Z(\boldsymbol{p}_0) \tag{2}$$

The general knowledge base of $X(\boldsymbol{p})$ includes the mean function $m_x(\boldsymbol{p}) = E[X]$, which is assumed to be zero, and the covariance function $c_x(\boldsymbol{p},\boldsymbol{p}') = E[(X(\boldsymbol{p}) - m(\boldsymbol{p}))(X(\boldsymbol{p}') - m(\boldsymbol{p}'))]$, which is determined by the experimental covariance of $\boldsymbol{x}_0$

$$\widehat{c_X}(r, \tau) \approx \frac{1}{N(r, \tau)} \sum_{i=1}^{N(r,\tau)} x_{\text{head},i}x_{\text{tail},i} - m_X^2 \tag{3}$$

where $N(r,\tau)$ is the number of pairs of points with values $(x_{\text{head}}, x_{\text{tail}})$ separated by a distance r and time τ, and m_x is the mean of $\boldsymbol{x}_0$. For the S/TRF $X(\boldsymbol{p})$, we use an exponential covariance model to best fit the experimental covariance

$$\begin{aligned}c_X(r, \tau) = C\Bigg[&\gamma \exp\frac{-3r}{a_{r1}}\exp\frac{-3\tau}{a_{t1}} + \lambda \exp\frac{-3r}{a_{r2}}\exp\frac{-3\tau}{a_{t2}}\\ &+ (1 - \gamma - \lambda)\exp\frac{-3r}{a_{r3}}\exp\frac{-3\tau}{a_{t3}}\Bigg]\end{aligned} \tag{4}$$

with parameters in the Supporting Information. The BME estimation process involves using general knowledge to obtain the maximum entropy prior probability density function (PDF) of f_G, updating f_G by integrating site-specific knowledge to obtain the epistemic Bayesian posterior PDF f_K, which provides a complete stochastic description of $X_k = X(\boldsymbol{p}_k)$ at the estimation point $\boldsymbol{p}_k$, and computing space−time estimates based on f_K. The posterior PDF is defined as

https://dx.doi.org/10.1021/acs.est.0c07742
Environ. Sci. Technol. 2021, 55, 4389−4398

$$f_K(x_k) = \left(\frac{f_G(x_0, x_k)}{f_G(x_0)} \right) \quad (5)$$

where x_k is the offset-removed estimate at points $\boldsymbol{p}_k$. We define the ozone S/TRF, $Z(\boldsymbol{p})$, as the sum of $X(\boldsymbol{p})$ and the offset (multimodel composite)

$$Z(\boldsymbol{p}) = X(\boldsymbol{p}) + o_z(\boldsymbol{p}) \quad (6)$$

We obtain the estimated OSDMA8 z_k at $\boldsymbol{p}_k$ by adding back $o_z(\boldsymbol{p}_k)$ to the BME estimate x_k for the S/TRF $X(\boldsymbol{p})$ at $\boldsymbol{p}_k$.

Fine Resolution Addition. We calculate ozone BME estimates at 0.5° resolution; however, a finer resolution is desirable for GBD to reduce spatial misalignment with population. Since neither the observations nor the models represent ozone at fine resolution, except where observations are dense, we use the spatial distribution of a fine resolution model. We use output from an NASA G5NR-Chem model[26] simulation from July 2013 to June 2014 at 0.125° resolution, which we regrid to 0.1° resolution, to provide the fine spatial structure within each 0.5° grid cell for each year from 1990 to 2017. While we do not expect the modeled 2013−2014 ozone to be accurate for every year, we use the modeled spatial distribution to inform the fine-scale spatial pattern for each year. In doing so, we assume that the fine spatial patterns of OSMDA8 do not change over time, as these reflect the spatial distributions of emissions and land use, as well as influences like topography and land/water interfaces. For each 0.5° grid cell, we subtract the average of NASA G5NR-Chem grid cells from the BME estimate and add this difference to each NASA G5NR-Chem grid cell at 0.1° to obtain our BME estimate at 0.1°. Consequently, the subgrid variability of the output matches the G5NR-Chem model, and the average of each 0.5° grid cell remains the same as the BME estimate (Figures S2 and S3).

RESULTS

Multimodel Composite. We determine weights for each model in each region and year (Table S1). In most of the regions and years, the multimodel mean ozone (the simple average of all models) is biased high, as models generally overpredict ozone.[8,18] Therefore, the M^{3}Fusion multimodel composite (Figure 2) tends to decrease average ozone compared to the multimodel mean.

BME Coarse Resolution Output. We obtain yearly ozone output at 0.5° resolution, with an associated variance at each estimation point (Figure 3 and Figures S4−S31). The ozone output matches an observation at its space−time location, and the observation's influence decreases in space and time according to the derived spatiotemporal covariance (equation S3). In regions with high observational coverage, there is greater spatial variation in output, whereas that of less monitored regions is smoother. Areas of low estimated ozone include the Amazon, Oceania, and southeastern Africa, while high ozone is estimated in East Asia, South-Central Asia, western North America, and central Africa. The Amazon and central Africa are unmonitored; therefore, their respective low and high ozone estimates are based on model output reflecting ozone chemical destruction and dry deposition over the Amazon[55] and biomass burning in Africa.[56]

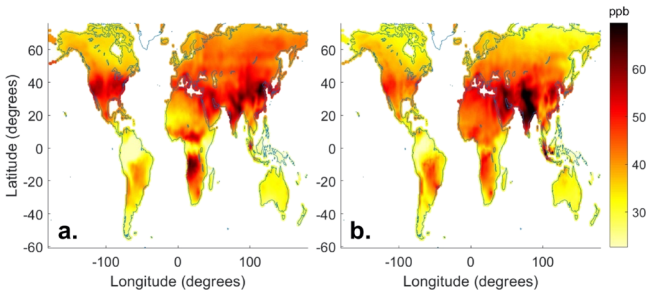

Figure 2. Multimodel composite as OSDMA8 in 2005 (a) and 2015 (b).

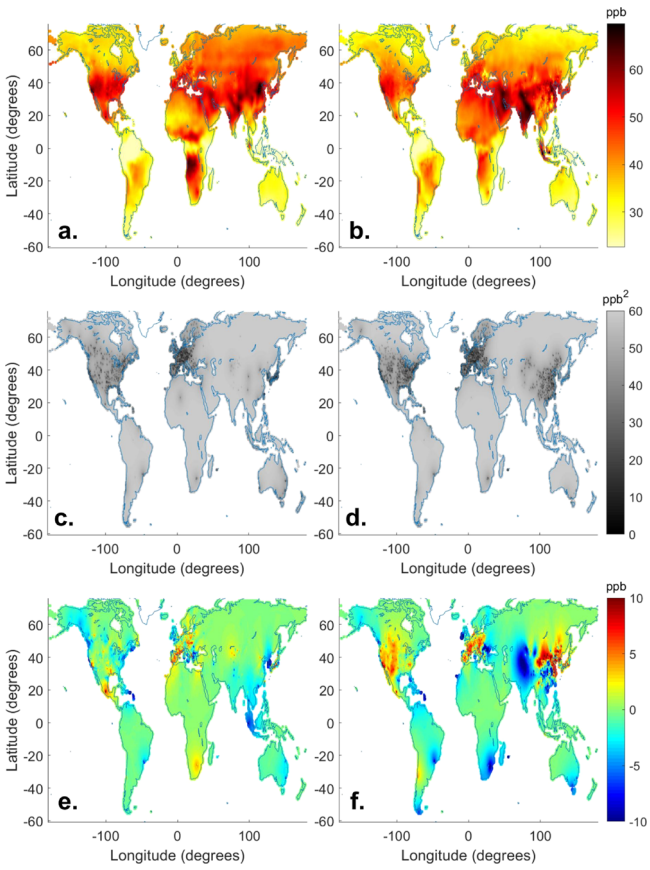

Figure 3. BME estimate as OSDMA8 for 2005 (a) and 2015 (b). BME variance for 2005 (c) and 2015 (d). Effect of BME fusion of observations (BME estimate minus the multimodel composite) for 2005 (e) and 2015 (f). Positive values occur where our estimate is higher than the multimodel composite and negative values where our estimate is lower.

In BME, observations are treated as hard data with no variance; therefore, regions with the highest number of observations have the lowest variance, such as North America, Europe, and Japan in 2005 and additionally eastern China in 2015. Away from observations, the output is equal to the multimodel composite, and the variance reaches a maximum of 60 ppb^2, equal to the variance of the offset-removed observations. To visualize how BME adjusted the multimodel composite using observations, we subtract the multimodel composite from our BME estimate (Figure 3). In unmonitored regions, there is no difference between our BME output and the multimodel composite. When adding fine resolution in the final step, differences on the global scale are unnoticeable (Figures S4−S31).

https://dx.doi.org/10.1021/acs.est.0c07742
Environ. Sci. Technol. 2021, 55, 4389−4398

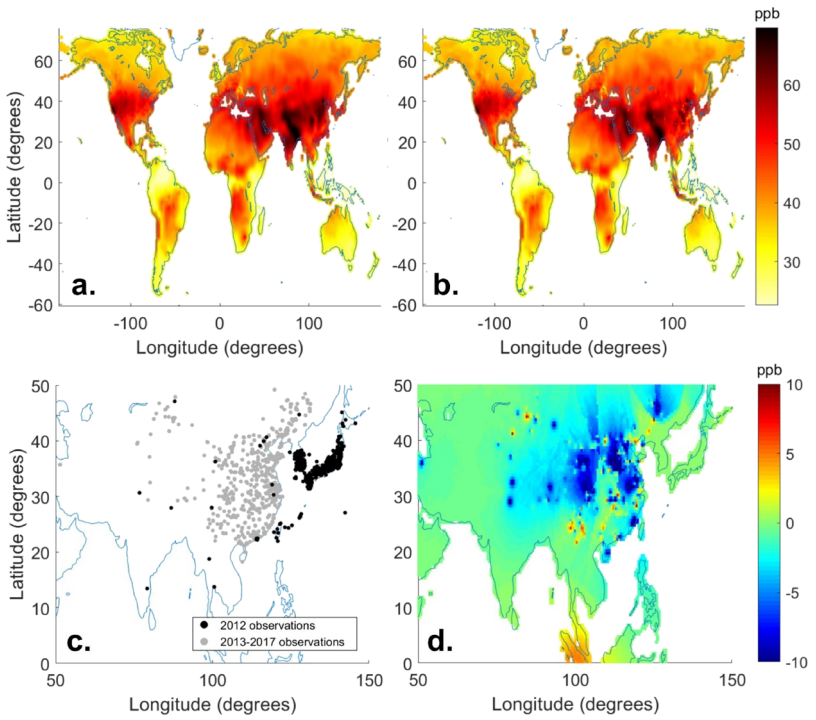

Figure 4. (a) Space-only BME result in 2012 as OSDMA8. (b) Space−time BME result in 2012 as OSDMA8. (c) Observation locations in 2012 and 2013−2017. (d) Effect of the BME space−time influence of observations (space−time BME minus the space-only BME) for 2012.

Influence of Observations through Time. The ability of observations to influence other years is an important component of our method since observational coverage changes, generally with more stations being added. The extent of an observation's influence on other years depends on the number of nearby stations in space and time, with more remote stations having a longer temporal influence. In addition to the space−time BME estimates above, we also perform "space-only" BME, in which observations only influence ozone estimates across space in a single year.

By taking the difference between space−time and space-only results, we evaluate how observations influence other years. Since the CNEMC observations started in 2013, analyzing 2012 highlights their temporal influence (Figure 4). On the global scale, differences between the space−time and space-only methods are difficult to distinguish, but major differences occur across China. Most of the nonzero differences occur in areas where CNEMC observations were added in 2013−2017, showing the influences of those observations (Figure 4). Whereas Figure 4 shows that BME largely decreased ozone estimates over China in 2012, the effect of adding BME differed among years, including increasing ozone in 2015 and 2016 (Figures S29 and S30).

Evaluation. To evaluate our results, we perform a leave one out cross validation (LOOCV), where one observation is removed, and we evaluate our ability to predict this observation, in five scenarios

- Multimodel mean: average of all model output available in a given year.
- Multimodel composite: combination of model output using M^{3}Fusion.
- Space-only correction: the BME-corrected multimodel composite where observations only influence across space in a single year.
- Space−time correction: the BME-corrected multimodel composite where observations influence across space and time.
- Fine resolution: space−time-corrected output with fine resolution from the NASA G5NR-Chem model.

LOOCV was performed using two methods: predicting ozone at the test point's grid cell and at the test point's specific space−time location. The grid cell prediction was performed to allow a fair comparison between scenarios, since the fine resolution addition is limited to predicting at the grid cell level, and to evaluate the benefit of increasing output resolution. When predicting at the test point's grid cell, each subsequent scenario improved performance, as shown by the root-mean-square error (RMSE) (Table 2). The multimodel composite outperforms the multimodel mean across all validation statistics. Correcting the multimodel composite across space using observations improves the results, which is further amplified by correcting across both space and time. Adding fine spatial structure, which gives our final output, slightly improves performance relative to the space−time scenario. All methods overestimate ozone in comparison to observations, as shown by the mean error (Table 2), though our final product is highly biased only slightly.

For comparison with other studies, we include statistics for predicting at the specific space−time location (Table 2). The addition of the space−time correction to the multimodel composite decreased RMSE from 7.82 to 3.99 ppb, a 49% reduction. In comparison, Chang et al.[18] report that the correction to the multimodel composite in that study decreased the RMSE from 5.16 to 3.82 ppb, a 26% reduction. The greater relative reduction in RMSE here is attributed to the incorporation of both spatial and temporal autocorrelation and shows our improvement relative to Chang et al.[18] (Figure S33).

https://dx.doi.org/10.1021/acs.est.0c07742
Environ. Sci. Technol. 2021, 55, 4389−4398

Table 2. LOOCV Statistics,[a] where Results Are Evaluated in the 0.5 or 0.1 Grid Cells Containing the Test Point or at the Test Point's Space−Time Location

scenario	prediction location	RMSE (ppb)	ME (ppb)	R^2	varE (ppb^2)	varZ (ppb^2)
multimodel mean	0.5° grid cell	13.76	11.00	0.28	68.48	62.08
multimodel composite	0.5° grid cell	7.82	1.05	0.30	60.03	43.09
space-only correction	0.5° grid cell	6.01	0.42	0.57	36.00	60.14
space−time correction	0.5° grid cell	5.62	0.57	0.62	31.30	62.01
fine resolution	0.1° grid cell	5.54	0.22	0.63	30.68	63.24
multimodel composite	test point's location	7.82	1.07	0.30	60.00	43.19
space−time correction	test point's location	3.99	0.01	0.81	15.94	81.26

[a]Root-mean-square error (RMSE), mean error (ME), *R*-squared (R^2), variance of error (varE), and variance of estimated ozone (varZ). The mean and variance of observed ozone are mO = 45.62 ppb and varO = 81.96 ppb^2, respectively. Statistic definitions are included in Table S2.

Population-Weighted Ozone Trends. We use global gridded population from GBD 2019 to analyze trends in population-weighted ozone as an indicator of exposure. The 2019 global population is used for all years, meaning that differences in exposure result from changes in ozone, not population. To determine how ozone exposure has changed from 1990 to 2017, we examine the percent of the global population exposed to intervals of OSDMA8 (Figure 5).

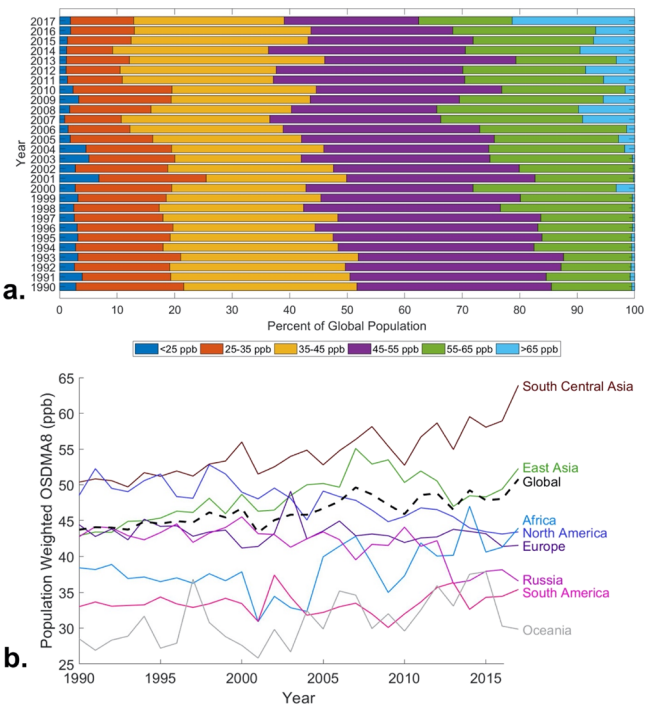

Figure 5. (a) Percent of the global population exposed to 10 ppb intervals of OSDMA8 from 1990 to 2017. (b) Ozone trend regionally (regions defined in Figure S1) over 1990−2017 for the metric of population-weighted OSDMA8. All trends have *p*-values less than 0.05, except for Europe and South America (Table S3). Uncertainty intervals are included in Figures S35−48.

Global ozone exposure increases over this period, with an increase in the global population exposed to the highest concentrations (>55 ppb). In 2017, 21.3% of the global population was exposed to OSDMA8 higher than 65 ppb, more than double the percentage in any previous year. Note that the OSDMA8 metric is not compared easily with national standards or WHO guidelines, which are typically based on the daily 8 h maximum. For perspective, the risk of all-cause, circulatory, and respiratory mortality reportedly increases by 2, 3, and 12% per 10 ppb increase in long-term OSDMA8, respectively, with some evidence that ozone influences mortality at concentrations above about 35 ppb.[2]

We analyze the population-weighted trends from 1990 to 2017 for each world region (Figure 5) and the most populous countries (Figure S34). Globally, there is a positive trend in population-weighted ozone for 1990−2017, driven in large part by positive trends in highly populated and polluted regions of South-Central Asia, East Asia, and Africa. Low population-weighted ozone occurs in South America and Oceania. Negative trends occur in North America and Russia; Europe has a weak negative trend, with the European Union showing no change. We caution that these trends are the most uncertain before 2000 and in regions with few observations; under these conditions, our estimated trends mainly reflect models and a small number of observations. Year-to-year changes in ozone in regions with few observations may also result from using different model weights in individual years. These trends are supported by a previous TOAR analysis of 2000−2014 summertime ozone, which found a positive trend in East Asia and negative trends in North America and Europe.[57] Similarly, a study of CNEMC observations showed increases in China for 2013−2017.[31] One study suggests that the 2013−2017 increase over China was influenced most by the decrease in $PM_{2.5}$, which increased HO_x radicals;[58] therefore, a $PM_{2.5}$ increase might explain our estimated 2007−2013 ozone decrease. Increasing trends in other regions with few observations, including Africa and South Central Asia, are supported by long-term aircraft[59] and satellite column observations.[47]

DISCUSSION

We create fine resolution yearly ozone distributions for 1990−2017 that incorporate surface observations and output from nine atmospheric chemistry models, using a novel combination of the M^{3}Fusion method for creating a multimodel composite, which dominates the large-scale ozone estimates, and BME data fusion, which influences ozone estimates near observation locations, smoothly integrating observations in space and time. We find that methods incorporating observations outperform ozone estimated from models only. Additionally, the influence of an observation across multiple years in BME further improves our ozone estimate. Our method's major strengths include the incorporation of multiple data types, the smooth weighting of the observational influence across space and time, the ability to output a variance at every estimation point, and the fine spatial structure. The improvement in model performance from using our combination of M^{3}Fusion and BME provides a caution against using simple spatial interpolations of observations or output of a model without bias correction to represent ozone. Although we improve upon the previous GBD ozone estimate, some limitations remain. The lack of monitoring stations in large populous regions limits our abilities to understand ozone exposure in these areas,

https://dx.doi.org/10.1021/acs.est.0c07742
Environ. Sci. Technol. 2021, 55, 4389−4398

where these uncertainties affect both the multimodel composite and BME data fusion. Our method is limited in years with fewer observations and models available; additionally, the fine resolution model output that informs the fine spatial pattern of our output is only available for a single year. Future work may apply a nonlinear bias correction, or use machine learning to correct bias,[60] to the multimodel composite to improve the global offset and thus the overall estimation. Our work also shows the value of using multiple models in creating a multimodel composite, as output from each model was selected (weight > 0) in at least some regions and years.

Our method can be applied to future years as more observations and model output become available. Additionally, our method can be used to estimate ozone metrics other than OSDMA8, including for studies of vegetation and crop impacts.[61] While model output and geostatistical techniques like BME can estimate global ozone, estimates suffer from the lack of observations in some world regions. Additional observations, especially in unmonitored regions with large populations including megacities in low- and middle-income nations, are essential to improve the understanding of ozone exposure and health burden.

Ozone exposure is increasing globally, with global population-weighted ozone showing a positive trend from 1990 to 2017, driven by strong positive trends in highly populated and polluted regions of Asia and Africa. The increasing global exposure to ozone indicates that current ozone management policies are failing to reduce ozone exposure in many regions. Our results can be used by policy makers to identify regions where ozone pollution could be mitigated through reductions of ozone precursor emissions, mainly from fossil fuel combustion, on local, national, and continental scales, or through international agreements to reduce emissions, including methane, that affect global background ozone.[62,63]

■ ASSOCIATED CONTENT

Supporting Information

The Supporting Information is available free of charge at https://pubs.acs.org/doi/10.1021/acs.est.0c07742.

Multimodel composite model weights, covariance parameters, fine resolution addition examples, yearly maps for all relevant scenarios, cross validation statistics, and national ozone trends with uncertainty intervals (PDF)

■ AUTHOR INFORMATION

Corresponding Author

J. Jason West − *Department of Environmental Sciences and Engineering, University of North Carolina at Chapel Hill, Chapel Hill, North Carolina 27599, United States;* orcid.org/0000-0001-5652-4987; Phone: 919-843-3928; Email: jasonwest@unc.edu

Authors

Marissa N. DeLang − *Department of Environmental Sciences and Engineering, University of North Carolina at Chapel Hill, Chapel Hill, North Carolina 27599, United States*

Jacob S. Becker − *Department of Environmental Sciences and Engineering, University of North Carolina at Chapel Hill, Chapel Hill, North Carolina 27599, United States*

Kai-Lan Chang − *Cooperative Institute for Research in Environmental Sciences, University of Colorado, Boulder, Colorado 80309-0401, United States; NOAA Chemical Sciences Laboratory, Boulder, Colorado 80305, United States*

Marc L. Serre − *Department of Environmental Sciences and Engineering, University of North Carolina at Chapel Hill, Chapel Hill, North Carolina 27599, United States*

Owen R. Cooper − *Cooperative Institute for Research in Environmental Sciences, University of Colorado, Boulder, Colorado 80309-0401, United States; NOAA Chemical Sciences Laboratory, Boulder, Colorado 80305, United States*

Martin G. Schultz − *Jülich Supercomputing Centre (JSC), Forschungszentrum Jülich, Jülich D-5242, Germany*

Sabine Schröder − *Jülich Supercomputing Centre (JSC), Forschungszentrum Jülich, Jülich D-5242, Germany*

Xiao Lu − *Laboratory for Climate and Ocean-Atmosphere Studies, Department of Atmospheric and Oceanic Sciences, School of Physics, Peking University, Beijing 100871, China;* orcid.org/0000-0002-5989-0912

Lin Zhang − *Laboratory for Climate and Ocean-Atmosphere Studies, Department of Atmospheric and Oceanic Sciences, School of Physics, Peking University, Beijing 100871, China;* orcid.org/0000-0003-2383-8431

Makoto Deushi − *Meteorological Research Institute (MRI), Tsukuba 305-0052, Japan*

Beatrice Josse − *Centre National de Recherches Météorologiques, Université de Toulouse, Météo-France, CNRS, Toulouse 31057, France*

Christoph A. Keller − *NASA Goddard Space Flight Center, Greenbelt, Maryland 20771-0003, United States; Universities Space Research Association, Columbia, Maryland 21046, United States*

Jean-François Lamarque − *National Center for Atmospheric Research, Boulder, Colorado 80305, United States*

Meiyun Lin − *NOAA Geophysical Fluid Dynamics Laboratory, Princeton, New Jersey 08540, United States; Program in Atmospheric and Oceanic Sciences, Princeton University, Princeton, New Jersey 08544, United States*

Junhua Liu − *NASA Goddard Space Flight Center, Greenbelt, Maryland 20771-0003, United States; Universities Space Research Association, Columbia, Maryland 21046, United States*

Virginie Marécal − *Centre National de Recherches Météorologiques, Université de Toulouse, Météo-France, CNRS, Toulouse 31057, France*

Sarah A. Strode − *NASA Goddard Space Flight Center, Greenbelt, Maryland 20771-0003, United States; Universities Space Research Association, Columbia, Maryland 21046, United States*

Kengo Sudo − *Graduate School of Environmental Studies, Nagoya University, Nagoya 464-8601, Japan; Japan Agency for Marine-Earth Science and Technology (JAMSTEC), Yokosuka 237-0061, Japan*

Simone Tilmes − *National Center for Atmospheric Research, Boulder, Colorado 80305, United States*

Li Zhang − *NOAA Geophysical Fluid Dynamics Laboratory, Princeton, New Jersey 08540, United States; Program in Atmospheric and Oceanic Sciences, Princeton University, Princeton, New Jersey 08544, United States; Department of Meteorology and Atmospheric Science, Pennsylvania State University, University Park, Pennsylvania 16802-1503, United States;* orcid.org/0000-0003-0343-9476

https://dx.doi.org/10.1021/acs.est.0c07742
Environ. Sci. Technol. 2021, 55, 4389−4398

Stephanie E. Cleland − *Department of Environmental Sciences and Engineering, University of North Carolina at Chapel Hill, Chapel Hill, North Carolina 27599, United States*

Elyssa L. Collins − *Department of Environmental Sciences and Engineering, University of North Carolina at Chapel Hill, Chapel Hill, North Carolina 27599, United States*

Michael Brauer − *Institute for Health Metrics and Evaluation, University of Washington, Seattle, Washington 98195, United States; School of Population and Public Health, University of British Columbia, Vancouver, British Columbia V6T 1Z3, Canada;* orcid.org/0000-0002-9103-9343

Complete contact information is available at: https://pubs.acs.org/10.1021/acs.est.0c07742

Notes

The authors declare no competing financial interest.

■ ACKNOWLEDGMENTS

We acknowledge support from the NASA Health and Air Quality Applied Sciences Team (#NNX16AQ30G) and the National Institute for Occupational Safety and Health (T42-OH008673). M.D. was supported by the Japan Society for the Promotion of Science (JP20K04070).

■ REFERENCES

(1) Jerrett, M.; Burnett, R. T.; Pope, C. A., III; Ito, K.; Thurston, G.; Krewski, D.; Shi, Y.; Calle, E.; Thun, M. Long-Term Ozone Exposure and Mortality. *N. Engl. J. Med.* **2009**, *360*, 1085−1095.

(2) Turner, M. C.; Jerrett, M.; Pope, C. A., III; Krewski, D.; Gapstur, S. M.; Diver, W. R.; Beckerman, B. S.; Marshall, J. D.; Su, J.; Crouse, D. L.; Burnett, R. T. Long-Term Ozone Exposure and Mortality in a Large Prospective Study. *Am. J. Respir. Crit. Care Med.* **2016**, *193*, 1134−1142.

(3) Di, Q.; Dai, L.; Wang, Y.; Zanobetti, A.; Choirat, C.; Schwartz, J. D.; Dominici, F. Association of short-term exposure to air pollution with mortality in older adults. *JAMA.* **2017**, *318*, 2446−2456.

(4) Myhre, G.; Shindell, D.; Bréon, F.-M.; Collins, W.; Fuglestvedt, J.; Huang, J.; Koch, D.; Lamarque, J.-F.; Lee, D.; Mendoza, B.; Nakajima, T.; Robock, A.; Stephens, G.; Takemura, T.; Zhang, H. Anthropogenic and Natural Radiative Forcing. In *Climate Change 2013: The Physical Science Basis. Contribution of Working Group I to the Fifth Assessment Report of the Intergovernmental Panel on Climate Change*; Stocker, T. F., Qin, D., Plattner, G.-K., Tignor, M. M. B., Allen, S. K., Boschung, J., Nauels, A., Xia, Y., Bex, V., Midgley, P. M., Eds.; Cambridge University Press: Cambridge, United Kingdom and New York, NY, USA, 2013.

(5) U.S. EPA *Integrated Science Assessment for Ozone and Related Photochemical Oxidants*; U.S. Environmental Protection Agency: Washington, DC, EPA/600/R-20/012, 2020.

(6) Emberson, L. D.; Pleijel, H.; Ainsworth, E. A.; van den Berg, M.; Ren, W.; Osborne, S.; Mills, G.; Pandey, D.; Dentener, F.; Büker, P.; Ewert, F.; Koeble, R.; Van Dingenen, R. Ozone Effects on Crops and Consideration in Crop Models. *Eur. J. Agron.* **2018**, *100*, 19−34.

(7) Fleming, Z. L.; Doherty, R. M.; Von Schneidemesser, E.; Malley, C. S.; Cooper, O. R.; Pinto, J. P.; Colette, A.; Xu, X.; Simpson, D.; Schultz, M. G.; Lefohn, A. S.; Hamad, S.; Moolla, R.; Solberg, S.; Feng, Z. Tropospheric Ozone Assessment Report: Present-Day Ozone Distribution and Trends Relevant to Human Health. *Elem. Sci. Anthropocene* **2018**, *6*, 12.

(8) Cooper, O. R.; Parrish, D. D.; Ziemke, J.; Balashov, N. V.; Cupeiro, M.; Galbally, I. E.; Gilge, S.; Horowitz, L.; Jensen, N. R.; Lamarque, J.-F.; Naik, V.; Oltmans, S. J.; Schwab, J.; Shindell, D. T.; Thompson, A. M.; Thouret, V.; Wang, Y.; Zbinden, R. M. Global Distribution and Trends of Tropospheric Ozone: An Observation-Based Review. *Elem. Sci. Anthropocene* **2014**, *2*, No. 000029.

(9) Lim, S. S.; Vos, T.; Flaxman, A. D.; Danaei, G.; Shibuya, K.; Adair-Rohani, H.; AlMazroa, M. A.; Amann, M.; Anderson, H. R.; Andrews, K. G.; et al. A Comparative Risk Assessment of Burden of Disease and Injury Attributable to 67 Risk Factors and Risk Factor Clusters in 21 Regions, 1990-2010: A Systematic Analysis for the Global Burden of Disease Study 2010. *Lancet* **2012**, *380*, 2224−2260.

(10) Cohen, A. J.; Brauer, M.; Burnett, R.; Anderson, H. R.; Frostad, J.; Estep, K.; Balakrishnan, K.; Brunekreef, B.; Dandona, L.; Dandona, R.; Feigin, V.; Freedman, G.; Hubbell, B.; Jobling, A.; Kan, H.; Knibbs, L.; Liu, Y.; Martin, R.; Morawska, L.; Pope, C. A., III; Shin, H.; Straif, K.; Shaddick, G.; Thomas, M.; van Dingenen, R.; van Donkelaar, A.; Vos, T.; Murray, C. J. L.; Forouzanfar, M. H. Estimates and 25-Year Trends of the Global Burden of Disease Attributable to Ambient Air Pollution: An Analysis of Data from the Global Burden of Diseases Study 2015. *Lancet* **2017**, *389*, 1907−1918.

(11) Shaddick, G.; Thomas, M. L.; Green, A.; Brauer, M.; van Donkelaar, A.; Burnett, R.; Chang, H. H.; Cohen, A.; Van Dingenen, R.; Dora, C.; Gumy, S.; Liu, Y.; Martin, R.; Waller, L. A.; West, J.; Zidek, J. V.; Prüss-Ustün, A. Data Integration Model for Air Quality: A Hierarchical Approach to the Global Estimation of Exposures to Ambient Air Pollution. *J. R. Stat. Soc. Ser. C Appl. Stat.* **2018**, *67*, 231−253.

(12) Shaddick, G.; Thomas, M. L.; Amini, H.; Broday, D.; Cohen, A.; Frostad, J.; Green, A.; Gumy, S.; Liu, Y.; Martin, R. V.; Pruss-Ustun, A.; Simpson, D.; van Donkelaar, A.; Brauer, M. Data Integration for the Assessment of Population Exposure to Ambient Air Pollution for Global Burden of Disease Assessment. *Environ. Sci. Technol.* **2018**, *52*, 9069−9078.

(13) Stanaway, J. D.; Afshin, A.; Gakidou, E.; Lim, S. S.; Abate, D.; Abate, K. H.; Abbafati, C.; Abbasi, N.; Abbastabar, H.; Abd-Allah, F.; et al. Global, Regional, and National Comparative Risk Assessment of 84 Behavioural, Environmental and Occupational, and Metabolic Risks or Clusters of Risks for 195 Countries and Territories, 1990-2017: A Systematic Analysis for the Global Burden of Disease Study 2017. *Lancet* **2018**, *392*, 1923−1994.

(14) Brauer, M.; Freedman, G.; Frostad, J.; van Donkelaar, A.; Martin, R. V.; Dentener, F.; Dingenen, R.; Estep, K.; Amini, H.; Apte, J. S.; Balakrishnan, K.; Barregard, L.; Broday, D.; Feigin, V.; Ghosh, S.; Hopke, P. K.; Knibbs, L. D.; Kokubo, Y.; Liu, Y.; Ma, S.; Morawska, L.; Sangrador, J. L. T.; Shaddick, G.; Anderson, H. R.; Vos, T.; Forouzanfar, M. H.; Burnett, R. T.; Cohen, A. Ambient Air Pollution Exposure Estimation for the Global Burden of Disease 2013. *Environ. Sci. Technol.* **2016**, *50*, 79−88.

(15) Gaudel, A.; Cooper, O. R.; Ancellet, G.; Barret, B.; Boynard, A.; Burrows, J. P.; Clerbaux, C.; Coheur, P. F.; Cuesta, J.; Cuevas, E.; Doniki, S.; Dufour, G.; Ebojie, F.; Foret, G.; Garcia, O.; Granados-Muñoz, M. J.; Hannigan, J. W.; Hase, F.; Hassler, B.; Huang, G.; Hurtmans, D.; Jaffe, D.; Jones, N.; Kalabokas, P.; Kerridge, B.; Kulawik, S.; Latter, B.; Leblanc, T.; le Flochmoën, E.; Lin, W.; Liu, J.; Liu, X.; Mahieu, E.; McClure-Begley, A.; Neu, J. L.; Osman, M.; Palm, M.; Petetin, H.; Petropavlovskikh, I.; Querel, R.; Rahpoe, N.; Rozanov, A.; Schultz, M. G.; Schwab, J.; Siddans, R.; Smale, D.; Steinbacher, M.; Tanimoto, H.; Tarasick, D. W.; Thouret, V.; Thompson, A. M.; Trickl, T.; Weatherhead, E.; Wespes, C.; Worden, H. M.; Vigouroux, C.; Xu, X.; Zeng, G.; Ziemke, J. Tropospheric Ozone Assessment Report: Present-Day Distribution and Trends of Tropospheric Ozone Relevant to Climate and Global Atmospheric Chemistry Model Evaluation. *Elem. Sci. Anthropocene* **2018**, *6*, 39.

(16) Schultz, M. G.; Schröder, S.; Lyapina, O.; Cooper, O.; Galbally, I.; Petropavlovskikh, I.; Von Schneidemesser, E.; Tanimoto, H.; Elshorbany, Y.; Naja, M.; Seguel, R.; Dauert, U.; Eckhardt, P.; Feigenspahn, S.; Fiebig, M.; Hjellbrekke, A.-G.; Hong, Y.-D.; Christian Kjeld, P.; Koide, H.; Lear, G.; Tarasick, D.; Ueno, M.; Wallasch, M.; Baumgardner, D.; Chuang, M.-T.; Gillett, R.; Lee, M.; Molloy, S.; Moolla, R.; Wang, T.; Sharps, K.; Adame, J. A.; Ancellet, G.; Apadula, F.; Artaxo, P.; Barlasina, M.; Bogucka, M.; Bonasoni, P.; Chang, L.; Colomb, A.; Cuevas, E.; Cupeiro, M.; Degorska, A.; Ding, A.; Fröhlich, M.; Frolova, M.; Gadhavi, H.; Gheusi, F.; Gilge, S.; Gonzalez, M. Y.; Gros, V.; Hamad, S. H.; Helmig, D.; Henriques, D.;

Hermansen, O.; Holla, R.; Huber, J.; Im, U.; Jaffe, D. A.; Komala, N.; Kubistin, D.; Lam, K.-S.; Laurila, T.; Lee, H.; Levy, I.; Mazzoleni, C.; Mazzoleni, L.; McClure-Begley, A.; Mohamad, M.; Murovic, M.; Navarro-Comas, M.; Nicodim, F.; Parrish, D.; Read, K. A.; Reid, N.; Ries, L.; Saxena, P.; Schwab, J. J.; Scorgie, Y.; Senik, I.; Simmonds, P.; Sinha, V.; Skorokhod, A.; Spain, G.; Spangl, W.; Spoor, R.; Springston, S. R.; Steer, K.; Steinbacher, M.; Suharguniyawan, E.; Torre, P.; Trickl, T.; Weili, L.; Weller, R.; Xu, X.; Xue, L.; Zhiqiang, M. Tropospheric Ozone Assessment Report: Database and Metrics Data of Global Surface Ozone Observations. *Elem. Sci. Anthropocene* **2017**, *5*, 58.

(17) Morgenstern, O.; Hegglin, M.; Rozanov, E.; O'Connor, F. M.; Abraham, N. L.; Akiyoshi, H.; Archibald, A.; Bekki, S.; Butchart, N.; Chipperfield, M.; Deushi, M.; Dhomse, S.; Garcia, R.; Hardiman, S.; Horowitz, L.; Jöckel, P.; Josse, B.; Kinnison, D.; Lin, M.; Mancini, E.; Manyin, M.; Marchand, M.; Marécal, V.; Michou, M.; Oman, L.; Pitari, G.; Plummer, D.; Revell, L.; Saint-Martin, D.; Schofield, R.; Stenke, A.; Stone, K.; Sudo, K.; Tanaka, T.; Tilmes, S.; Yamashita, Y.; Yoshida, K.; Zeng, G. Review of the Global Models Used within Phase 1 of the Chemistry-Climate Model Initiative (CCMI). *Geosci. Model Dev.* **2017**, *10*, 639−671.

(18) Chang, K.-L.; Cooper, O. R.; West, J. J.; Serre, M. L.; Schultz, M. G.; Lin, M.; Marécal, V.; Josse, B.; Deushi, M.; Sudo, K.; Liu, J.; Keller, C. A. A New Method (M^3Fusion v1) for Combining Observations and Multiple Model Output for an Improved Estimate of the Global Surface Ozone Distribution. *Geosci. Model Dev.* **2019**, *12*, 955−978.

(19) Christakos, G. A Bayesian/Maximum-Entropy View to the Spatial Estimation Problem. *Math. Geol.* **1990**, *22*, 763−777.

(20) Christakos, G.; Bogaert, P.; Serre, M. L. *Temporal GIS : Advanced Functions for Field-Based Applications*; Springer: Berlin Heidelberg, 2001.

(21) Serre, M. L.; Christakos, G. Modern Geostatistics: Computational BME Analysis in the Light of Uncertain Physical Knowledge - The Equus Beds Study. *Stoch. Environ. Res. Risk Assess.* **1999**, *13*, 1−26.

(22) Christakos, G.; Kolovos, A.; Serre, M. L.; Vukovich, F. Total Ozone Mapping by Integrating Databases from Remote Sensing Instruments and Empirical Models. *IEEE Trans. Geosci. Electron.* **2004**, *42*, 991−1008.

(23) De Nazelle, A.; Arunachalam, S.; Serre, M. L. Bayesian Maximum Entropy Integration of Ozone Observations and Model Predictions: An Application for Attainment Demonstration in North Carolina. *Environ. Sci. Technol.* **2010**, *44*, 5707−5713.

(24) Xu, Y.; Serre, M. L.; Reyes, J.; Vizuete, W. Bayesian Maximum Entropy Integration of Ozone Observations and Model Predictions: A National Application. *Environ. Sci. Technol.* **2016**, *50*, 4393−4400.

(25) Xu, Y.; Serre, M. L.; Reyes, J. M.; Vizuete, W. Impact of Temporal Upscaling and Chemical Transport Model Horizontal Resolution on Reducing Ozone Exposure Misclassification. *Atmos. Environ.* **2017**, *166*, 374−382.

(26) Hu, L.; Keller, C. A.; Long, M. S.; Sherwen, T.; Auer, B.; Da Silva, A.; Nielsen, J. E.; Pawson, S.; Thompson, M. A.; Trayanov, A. L.; Travis, K. R.; Grange, S. K.; Evans, M. J.; Jacob, D. J. Global Simulation of Tropospheric Chemistry at 12.5 Km Resolution: Performance and Evaluation of the GEOS-Chem Chemical Module (V10-1) within the NASA GEOS Earth System Model (GEOS-5 ESM). *Geosci. Model Dev.* **2018**, *11*, 4603−4620.

(27) Murray, C. J. L.; Aravkin, A. Y.; Zheng, P.; Abbafati, C.; Abbas, K. M.; Abbasi-Kangevari, M.; Abd-Allah, F.; Abdelalim, A.; Abdollahi, M.; Abdollahpour, I.; et al. Global Burden of 87 Risk Factors in 204 Countries and Territories, 1990−2019: A Systematic Analysis for the Global Burden of Disease Study 2019. *Lancet* **2020**, *396*, 1223−1249.

(28) Seltzer, K. M.; Shindell, D. T.; Kasibhatla, P.; Malley, C. S. Magnitude, Trends, and Impacts of Ambient Long-Term Ozone Exposure in the United States from 2000 to 2015. *Atmos. Chem. Phys.* **2020**, *20*, 1757−1775.

(29) Kleinert, F.; Leufen, L. H.; Schultz, M. G. IntelliO3-Ts v1.0: A Neural Network Approach to Predict near-Surface Ozone Concentrations in Germany. *Geosci. Model Dev.* **2021**, *14*, 1−25.

(30) Schultz, M. G.; Schröder, S.; Lyapina, O.; Cooper, O. R.; Galbally, I.; Petropavlovskikh, I.; von Schneidemesser, E.; Tanimoto, H.; Elshorbany, Y.; Naja, M.; Seguel, R. J.; Dauert, U.; Eckhardt, P.; Feigenspan, S.; Fiebig, M.; Hjellbrekke, A.-G.; Hong, Y.-D.; Kjeld, P. C.; Koide, H.; Lear, G.; Tarasick, D.; Ueno, M.; Wallasch, M.; Baumgardner, D.; Chuang, M.-T.; Gillett, R.; Lee, M.; Molloy, S.; Moolla, R.; Wang, T.; Sharps, K.; Adame, J. A.; Ancellet, G.; Apadula, F.; Artaxo, P.; Barlasina, M. E.; Bogucka, M.; Bonasoni, P.; Chang, L.; Colomb, A.; Cuevas-Agulló, E.; Cupeiro, M.; Degorska, A.; Ding, A.; Fröhlich, M.; Frolova, M.; Gadhavi, H.; Gheusi, F.; Gilge, S.; Gonzalez, M. Y.; Gros, V.; Hamad, S. H.; Helmig, D.; Henriques, D.; Hermansen, O.; Holla, R.; Hueber, J.; Im, U.; Jaffe, D. A.; Komala, N.; Kubistin, D.; Lam, K.-S.; Laurila, T.; Lee, H.; Levy, I.; Mazzoleni, C.; Mazzoleni, L. R.; McClure-Begley, A.; Mohamad, M.; Murovec, M.; Navarro-Comas, M.; Nicodim, F.; Parrish, D.; Read, K. A.; Reid, N.; Ries, L.; Saxena, P.; Schwab, J. J.; Scorgie, Y.; Senik, I.; Simmonds, P.; Sinha, V.; Skorokhod, A. I.; Spain, G.; Spangl, W.; Spoor, R.; Springston, S. R.; Steer, K.; Steinbacher, M.; Suharguniyawan, E.; Torre, P.; Trickl, T.; Weili, L.; Weller, R.; Xu, X.; Xue, L.; Zhiqiang, M. Tropospheric Ozone Assessment Report, Links to Global Surface Ozone Datasets. *PANGAEA* **2017**, 7.

(31) Lu, X.; Hong, J.; Zhang, L.; Cooper, O. R.; Schultz, M. G.; Xu, X.; Wang, T.; Gao, M.; Zhao, Y.; Zhang, Y. Severe Surface Ozone Pollution in China: A Global Perspective. *Environ. Sci. Technol. Lett.* **2018**, *5*, 487−494.

(32) Orbe, C.; Plummer, D. A.; Waugh, D. W.; Yang, H.; Jöckel, P.; Kinnison, D. E.; Josse, B.; Marecal, V.; Deushi, M.; Abraham, N. L.; Archibald, A. T.; Chipperfield, M. P.; Dhomse, S.; Feng, W.; Bekki, S. Description and Evaluation of the Specified-Dynamics Experiment in the Chemistry-Climate Model Initiative. *Atmos. Chem. Phys.* **2020**, *20*, 3809−3840.

(33) Lamarque, J.-F.; Bond, T. C.; Eyring, V.; Granier, C.; Heil, A.; Klimont, Z.; Lee, D.; Liousse, C.; Mieville, A.; Owen, B.; Schultz, M. G.; Shindell, D.; Smith, S. J.; Stehfest, E.; Van Aardenne, J.; Cooper, O. R.; Kainuma, M.; Mahowald, N.; McConnell, J. R.; Naik, V.; Riahi, K.; van Vuuren, D. P. Historical (1850−2000) Gridded Anthropogenic and Biomass Burning Emissions of Reactive Gases and Aerosols: Methodology and Application. *Atmos. Chem. Phys.* **2010**, *10*, 7017−7039.

(34) Granier, C.; Bessagnet, B.; Bond, T.; D'Angiola, A.; van der Gon, H. D.; Frost, G. J.; Heil, A.; Kaiser, J. W.; Kinne, S.; Klimont, Z.; Kloster, S.; Lamarque, J.-F.; Liousse, C.; Masui, T.; Meleux, F.; Mieville, A.; Ohara, T.; Raut, J.-C.; Riahi, K.; Schultz, M. G.; Smith, S. J.; Thompson, A.; van Aardenne, J.; van der Werf, G. R.; van Vuuren, D. P. Evolution of Anthropogenic and Biomass Burning Emissions of Air Pollutants at Global and Regional Scales during the 1980-2010 Period. *Clim. Change* **2011**, *109*, 163−190.

(35) Eyring, V.; Bony, S.; Meehl, G. A.; Senior, C. A.; Stevens, B.; Stouffer, R. J.; Taylor, K. E. Overview of the Coupled Model Intercomparison Project Phase 6 (CMIP6) Experimental Design and Organization. *Geosci. Model Dev.* **2016**, *9*, 1937−1958.

(36) Tilmes, S.; Lamarque, J.-F.; Emmons, L. K.; Kinnison, D. E.; Ma, P.-L.; Liu, X.; Ghan, S.; Bardeen, C.; Arnold, S.; Deeter, M.; Vitt, F.; Ryerson, T.; Elkins, J. W.; Moore, F.; Spackman, J. R.; Val Martin, M. Description and Evaluation of Tropospheric Chemistry and Aerosols in the Community Earth System Model (CESM1.2). *Geosci. Model Dev.* **2015**, *8*, 1395−1426.

(37) Garcia, R. R.; Smith, A. K.; Kinnison, D. E.; de la Cámara, Á.; Murphy, D. J. Modification of the Gravity Wave Parameterization in the Whole Atmosphere Community Climate Model: Motivation and Results. *J. Atmos. Sci.* **2017**, *74*, 275−291.

(38) Marsh, D. R.; Mills, M. J.; Kinnison, D. E.; Lamarque, J.-F.; Calvo, N.; Polvani, L. M. Climate Change from 1850 to 2005 Simulated in CESM1(WACCM). *J. Clim.* **2013**, *26*, 7372−7391.

https://dx.doi.org/10.1021/acs.est.0c07742
Environ. Sci. Technol. 2021, 55, 4389−4398

(39) Sudo, K.; Takahashi, M.; Kurokawa, J.-I.; Akimoto, H. CHASER: A Global Chemical Model of the Troposphere 1. Model Description. *J. Geophys. Res. Atmos.* **2002**, *107*, ACH 7-1−ACH 7-20.
(40) Sudo, K.; Takahashi, M.; Akimoto, H. CHASER: A Global Chemical Model of the Troposphere 2. Model Results and Evaluation. *J. Geophys. Res. Atmos.* **2002**, *107*, ACH 9-1−ACH 9-39.
(41) Watanabe, S.; Hajima, T.; Sudo, K.; Nagashima, T.; Takemura, T.; Okajima, H.; Nozawa, T.; Kawase, H.; Abe, M.; Yokohata, T.; Ise, T.; Sato, H.; Kato, E.; Takata, K.; Emori, S.; Kawamiya, M. MIROC-ESM 2010: Model Description and Basic Results of CMIP5-20c3m Experiments. *Geosci. Model Dev.* **2011**, *4*, 845−872.
(42) Lin, M.; Fiore, A. M.; Horowitz, L. W.; Cooper, O. R.; Naik, V.; Holloway, J.; Johnson, B. J.; Middlebrook, A. M.; Oltmans, S. J.; Pollack, I. B.; Ryerson, T. B.; Warner, J. X.; Wiedinmyer, C.; Wilson, J.; Wyman, B. Transport of Asian Ozone Pollution into Surface Air over the Western United States in Spring. *J. Geophys. Res. Atmos.* **2012**, *117* (), DOI: 10.1029/2011JD016961.
(43) Lin, M.; Horowitz, L. W.; Oltmans, S. J.; Fiore, A. M.; Fan, S. Tropospheric Ozone Trends at Mauna Loa Observatory Tied to Decadal Climate Variability. *Nat. Geosci.* **2014**, *7*, 136−143.
(44) Lin, M.; Horowitz, L. W.; Payton, R.; Fiore, A. M.; Tonnesen, G. US Surface Ozone Trends and Extremes from 1980 to 2014: Quantifying the Roles of Rising Asian Emissions, Domestic Controls, Wildfires, and Climate. *Atmos. Chem. Phys.* **2017**, *17*, 2943−2970.
(45) Zhang, L.; Lin, M.; Langford, A. O.; Horowitz, L. W.; Senff, C. J.; Klovenski, E.; Wang, Y.; Alvarez, R. J., II; Petropavlovskikh, I.; Cullis, P.; Sterling, C. W.; Peischl, J.; Ryerson, T. B.; Brown, S. S.; Decker, Z. C. J.; Kirgis, G.; Conley, S. Characterizing Sources of High Surface Ozone Events in the Southwestern US with Intensive Field Measurements and Two Global Models. *Atmos. Chem. Phys.* **2020**, *20*, 10379−10400.
(46) Horowitz, L. W.; Naik, V.; Paulot, F.; Ginoux, P. A.; Dunne, J. P.; Mao, J.; Schnell, J.; Chen, X.; He, J.; John, J. G.; Lin, M.; Lin, P.; Malyshev, S.; Paynter, D.; Shevliakova, E.; Zhao, M. The GFDL Global Atmospheric Chemistry-Climate Model AM4.1: Model Description and Simulation Characteristics. *J. Adv. Model. Earth Syst.* **2020**, *12*, No. e2019MS002032.
(47) Ziemke, J. R.; Oman, L. D.; Strode, S. A.; Douglass, A. R.; Olsen, M. A.; McPeters, R. D.; Bhartia, P. K.; Froidevaux, L.; Labow, G. J.; Witte, J. C.; Thompson, A. M.; Haffner, D. P.; Kramarova, N. A.; Frith, S. M.; Huang, L.-K.; Jaross, G. R.; Seftor, C. J.; Deland, M. T.; Taylor, S. L. Trends in Global Tropospheric Ozone Inferred from a Composite Record of TOMS/OMI/MLS/OMPS Satellite Measurements and the MERRA-2 GMI Simulation. *Atmos. Chem. Phys.* **2019**, *19*, 3257−3269.
(48) Strode, S. A.; Ziemke, J. R.; Oman, L. D.; Lamsal, L. N.; Olsen, M. A.; Liu, J. Global Changes in the Diurnal Cycle of Surface Ozone. *Atmos. Environ.* **2019**, *199*, 323−333.
(49) Josse, B.; Simon, P.; Peuch, V.-H. Radon Global Simulations with the Multiscale Chemistry and Transport Model MOCAGE. *Tellus B* **2004**, *56*, 339−356.
(50) Teyssèdre, H.; Michou, M.; Clark, H. L.; Josse, B.; Karcher, F.; Olivié, D.; Peuch, V.-H.; Saint-Martin, D.; Cariolle, D.; Attié, J.-L.; Nédélec, P.; Ricaud, P.; Thouret, V.; van der, A. R. J.; Volz-Thomas, A.; Chéroux, F. New Tropospheric and Stratospheric Chemistry and Transport Model MOCAGE-Climat for Multi-Year Studies: Evaluation of the Present-Day Climatology and Sensitivity to Surface Processes. *Atmos. Chem. Phys.* **2007**, *7*, 5815−5860.
(51) Adachi, Y.; Yukimoto, S.; Deushi, M.; Obata, A.; Nakano, H.; Tanaka, T.; Hosaka, M.; Sakami, T.; Yoshimura, H.; Hirabara, M.; Shindo, E.; Tsujino, H.; Mizuta, R.; Yabu, S.; Koshiro, T.; Ose, T.; Kitoh, A. Basic Performance of a New Earth System Model of the Meteorological Research Institute. *Pap. Meteorol. Geophys.* **2013**, *64*, 1−19.
(52) Yukimoto, S.; Kawai, H.; Koshiro, T.; Oshima, N.; Yoshida, K.; Urakawa, S.; Tsujino, H.; Deushi, M.; Tanaka, T.; Hosaka, M.; Yabu, S.; Yoshimura, H.; Shindo, E.; Mizuta, R.; Obata, A.; Adachi, Y.; Ishii, M. The Meteorological Research Institute Earth System Model Version 2.0, MRI-ESM2.0: Description and Basic Evaluation of the Physical Component. *J. Meteorol. Soc. Jpn.* **2019**, *97*, 931−965.
(53) Bolin, D.; Lindgren, F. Spatial Models Generated by Nested Stochastic Partial Differential Equations, with an Application to Global Ozone Mapping. *Ann. Appl. Stat.* **2011**, *5*, 523−550.
(54) Christakos, G. *Modern Spatiotemporal Geostatistics*; Oxford University Press: Cary, NC, 2000.
(55) Freire, L. S.; Gerken, T.; Ruiz-Plancarte, J.; Wei, D.; Fuentes, J. D.; Katul, G. G.; Dias, N. L.; Acevedo, O. C.; Chamecki, M. Turbulent Mixing and Removal of Ozone within an Amazon Rainforest Canopy. *J. Geophys. Res. Atmos.* **2017**, *122*, 2791−2811.
(56) Bauer, S. E.; Im, U.; Mezuman, K.; Gao, C. Y. Desert Dust, Industrialization, and Agricultural Fires: Health Impacts of Outdoor Air Pollution in Africa. *J. Geophys. Res. Atmos.* **2019**, *124*, 4104−4120.
(57) Chang, K.-L.; Petropavlovskikh, I.; Copper, O. R.; Schultz, M. G.; Wang, T. Regional Trend Analysis of Surface Ozone Observations from Monitoring Networks in Eastern North America, Europe and East Asia. *Elem. Sci. Anthropocene* **2017**, *5*, 50.
(58) Li, K.; Jacob, D. J.; Liao, H.; Shen, L.; Zhang, Q.; Bates, K. H. Anthropogenic Drivers of 2013−2017 Trends in Summer Surface Ozone in China. *Proc. Natl. Acad. Sci. U. S. A.* **2019**, *116*, 422−427.
(59) Gaudel, A.; Cooper, O. R.; Chang, K.-L.; Bourgeois, I.; Ziemke, J. R.; Strode, S. A.; Oman, L. D.; Sellitto, P.; Nédélec, P.; Blot, R.; Thouret, V.; Granier, C. Aircraft Observations since the 1990s Reveal Increases of Tropospheric Ozone at Multiple Locations across the Northern Hemisphere. *Sci. Adv.* **2020**, *6*, eaba8272.
(60) Ivatt, P. D.; Evans, M. J. Improving the Prediction of an Atmospheric Chemistry Transport Model Using Gradient-Boosted Regression Trees. *Atmos. Chem. Phys.* **2020**, *20*, 8063−8082.
(61) Mills, G.; Pleijel, H.; Malley, C. S.; Sinha, B.; Cooper, O. R.; Schultz, M. G.; Neufeld, H. S.; Simpson, D.; Sharps, K.; Feng, Z.; Gerosa, G.; Harmens, H.; Kobayashi, K.; Saxena, P.; Paoletti, E.; Sinha, V.; Xu, X. Tropospheric Ozone Assessment Report: Present-Day Tropospheric Ozone Distribution and Trends Relevant to Vegetation. *Elem. Sci. Anthropocene* **2018**, *6*, 47.
(62) West, J. J.; Fiore, A. M.; Horowitz, L. W.; Mauzerall, D. L. Global Health Benefits of Mitigating Ozone Pollution with Methane Emission Controls. *Proc. Natl. Acad. Sci. U. S. A.* **2006**, *103*, 3988−3993.
(63) Dentener, F.; Keating, T.; Akimoto, H. *Hemispheric Transport of Air Pollution: Part A: Ozone and Particulate Matter*; Economic Commission for Europe: Geneva, 2010.

https://dx.doi.org/10.1021/acs.est.0c07742
Environ. Sci. Technol. 2021, 55, 4389−4398